ISIJ International, Vol. 65 (2025), No. 10, pp. 1529–1540
https://doi.org/10.2355/isijinternational.ISIJINT-2025-211

Microstructure Development during Creep Deformation of 9Cr-1Mo-V-Nb Steel with Excess Nitrogen Introduced by Solution Nitriding – Multidimensional Scatter Diagram Analysis of STEM-EDS Maps by Machine Learning –

Tomotaka HATAKEYAMA,[1)]* Shuntaro IDA,[2)] Kota SAWADA[1)] and Kyosuke YOSHIMI[3)]

1) Research Center for Structural Materials, National Institute for Materials Science, 1-2-1, Sengen, Tsukuba, Ibaraki, 305-0047 Japan.
2) Department of Materials Science, Graduate School of Engineering, Tohoku University. Now at Materials Research and Development Laboratory, Japan Fine Ceramics Center, 2-4-1 Mutsuno, Atsuta-ku, Nagoya, 456-8587 Japan.
3) Department of Materials Science, Graduate School of Engineering, Tohoku University, 6-6-02, Aramaki Aza Aoba, Aoba-ku, Sendai, 980-8579 Japan.

(*Received June 17, 2025; Accepted July 16, 2025; Advance online published July 24, 2025; Published September 15, 2025; Originally published in Tetsu-to-Hagané, Vol. 111, 2025, No. 9, pp. 536–549*)

Creep deformation and precipitation behavior of 9Cr-1Mo-V-Nb steel with excess nitrogen introduced by solution nitriding were investigated. Precipitation of Cr_2N phase was confirmed in addition to $M_{23}C_6$ and MX phases in the tempered microstructure. The creep strength of the steel was significantly reduced by solution nitriding, while the creep rupture elongation was increased. To characterize the complex precipitation behavior of the nitrogen-added steel, a machine learning-based clustering method of the multidimensional scatter diagram of the X-ray intensity of the alloying elements in each pixel of a STEM-EDS map was developed. Reduced number density of precipitates and enhanced coarsening kinetics of both Cr_2N and MX were proposed as the mechanism of weakening caused by excess nitrogen.

KEY WORDS: nitrogen; precipitation; scatter diagram method; k-means clustering; creep deformation.

1. Introduction

9Cr-1Mo-V-Nb steel (KA-STPA28, ASME SA335M P91) is a ferritic heat-resistant steel commonly used for pipes in high-efficiency coal-fired power plants.[1)] To achieve carbon neutrality by 2050, the thermal power generation field is promoting the development of ammonia co- and mono-firing technology.[2)] In high-temperature environments, ammonia decomposes into hydrogen and nitrogen, with nitrogen penetrating into the material. Gas nitriding utilizes this phenomenon to achieve high hardness near the material surface through nitride formation.[3)] However, gas nitriding is conducted at approximately 773–873 K,[3)] which corresponds to the operating temperature range of 9Cr-1Mo-V-Nb steel, and steel materials used in an ammonia atmosphere for several decades may incur material property changes.

ASME SA335M P91[4)] specifies that the nitrogen content of 9Cr-1Mo-V-Nb steel is 0.030–0.070 mass%. Tsuchida *et al.*[5)] prepared 9Cr-1Mo-V-Nb steel with nitrogen contents ranging from 0.01 to 0.06 mass% via vacuum melting and investigated the effect of nitrogen content on creep rupture strength. A smaller nitrogen content resulted in finer and denser MX_n ($n \leq 1$) precipitation; thus, the creep strength on the short-term side of approximately 1 000 h was higher. As the nitrogen content increased, n increased and the thermodynamic stability of MX_n improved, indicating the likelihood that the creep strength on the long-term side of 20 000 h or more would be superior with a nitrogen content of 0.03 mass% or more.[5)] This nitrogen content corresponds to the lower limit of the standard.

To improve the properties of ferritic heat-resistant steel, research on the addition of nitrogen is also being conducted. The solubility of nitrogen in ferrite is approximately 0.1 mass%, making the addition of a large amount of nitrogen during melting difficult. Yamasaki *et al.*[6,7)] used the pressurized melting method to successfully add 0.3 mass% of nitrogen to 9Cr steel. However, during melting, coarse VN particles with a diameter of several micrometers were crystallized.[6,7)] Although the creep strength of the 9Cr steel with 0.3 mass% nitrogen was higher than that of 9Cr-1Mo-V-Nb steel at 923 K for times shorter than 500 h, the strength decreased at higher temperatures and longer times.[6)] Mean-

---

* Corresponding author: E-mail: hatakeyama.tomotaka@nims.go.jp

while, Matsubara *et al.* reported a significant improvement in the oxidation resistance of 9Cr steel through the addition of 0.3 mass% nitrogen using the pressurized melting method.[8]

Therefore, the purpose of this study is to investigate the creep deformation and precipitation behavior of 9Cr-1Mo-V-Nb steel owing to the addition of a large amount of nitrogen. Nitrogen addition was executed by heat-treating the steel under nitrogen atmosphere in the austenite single-phase region, where nitrogen solubility is high, using the solution-nitriding method to diffuse nitrogen from the material surface to the interior.[9–11] The solution-nitriding method is a solid-phase process and has the advantage of avoiding coarse VN particle crystallization. Nitrogen is supersaturated in martensite owing to martensitic transformation during cooling but is also expected to precipitate as nitrides via tempering.

Recently, data-driven material development is being strongly promoted in Japan.[12] The first step in digital transformation in structural materials is microstructure quantification. When considering the creep properties of heat-resistant steels, important features describing the microstructure include precipitate type, size, and number density. Although efforts have been made to extract features from grayscale microstructure images using machine learning,[13–16] distinguishing and extracting features from multiple types of fine precipitates in martensite solely from the contrast is difficult. Meanwhile, storing other descriptors such as chemical composition in each pixel of the microstructure image is thought to facilitate precipitate extraction. Therefore, in this study, we investigated a method for efficiently extracting and quantitatively evaluating fine precipitates based on the elemental map of 9Cr-1Mo-V-Nb steel, revealing complex precipitation behavior owing to nitrogen addition, and used this method to evaluate microstructural changes during creep.

2. Experimental Procedures

A pipe of 9Cr-1Mo-V-Nb steel was used as the test steel. **Table 1** lists the chemical composition of the as-received sample. A creep specimen with a gauge diameter of 6 mm and gauge length of 30 mm was used so that the longitudinal direction of the pipe was aligned with the stress direction. The samples for microstructural observation and creep testing were subjected to solution-nitriding heat treatment at 1 473 K for 48 h under nitrogen atmosphere of 1 atm.[17] The grain size of the prior austenite, coarsened as a result of the heat treatment, was adjusted by tempering at 1 033 K for 1 h, renormalizing at 1 323 K for 0.5 h, and tempering at 1 053 K for 1 h under nitrogen atmosphere of 1 atm.[18] After the heat treatment, the samples were cooled in a furnace. Henceforth, the samples that underwent the four-stage heat treatment shown in **Fig. 1** are referred to as solution-nitriding treated samples.

Creep testing of the solution-nitriding treated samples were conducted at 923 K in air at a constant load. The nominal stresses were 100, 80, and 70 MPa. The microstructure of the solution-nitriding treated samples before creep testing and after creep rupture were evaluated via scanning electron microscopy (SEM), electron backscatter diffraction (SEM-EBSD), scanning transmission electron microscopy (STEM), and energy dispersive X-ray spectroscopy (STEM-EDS). The samples for SEM observation were polished by buffing using colloidal silica. The thin films for STEM observation were prepared by twin-jet electrolytic polishing using a 10% perchloric acid-10% ethanol-80% glacial acetic acid solution. The data obtained by SEM-EBSD were analyzed using OIM-Analysis 8.6 (EDAX). The characteristic X-ray intensity data of nine elements, C, N, Si, V, Cr, Mn, Fe, Nb, and Mo, obtained by STEM-EDS with 256 × 256 points (= 65 536 points) were analyzed using Orange Data Mining.[19] The microstructure images were analyzed using Fiji.[20] Vickers hardness was measured at 5 kgf using samples for SEM observation. Five points were measured for each sample, and the average value of three points excluding the maximum and minimum values was taken as the Vickers hardness.

Table 1. Chemical composition of an as-received 9Cr-1Mo-V-Nb steel (mass%).

C	Cr	Mo	V	Nb	Mn	N	S	P	Si	Ni
0.09	8.58	0.94	0.21	0.07	0.35	0.04	<0.01	0.01	0.22	0.04

3. Results

3.1. Creep Properties of Solution-nitriding Treated Samples

Figure 2(a) shows the stress vs time to rupture time diagram of the solution-nitriding treated sample at 923 K obtained by creep testing. For comparison, results of the 9Cr-1Mo-V-Nb steel tubes (T91) and pipe (P91) reported in the NIMS creep datasheet[21] are also shown. The creep strength of the solution-nitriding treated sample was lower than the lower limit of the NIMS creep datasheet sample. Figures 2(b) and 2(c) show the relationship between the (b) creep rupture elongation and (c) reduction of area at rupture and the time to rupture obtained for the solution-nitriding treated sample at 923 K. Similar to Fig. 2(a), the results of the NIMS creep datasheet sample are shown for comparison.[21] The creep rupture elongation of the solution-nitriding treated sample was superior to the short-time side, that is, the high stress region, but the reduction of area at rupture was comparable to that of the NIMS creep datasheet sample.

Figure 3 shows the (a)–(c) strain vs time curves, (d)–(f) creep rate vs time curves, and (g)–(l) creep rate vs strain curves for each stress obtained for the solution-nitriding treated sample at 923 K by creep testing. The horizontal axis of (g)–(i) is linear, and the horizontal axis of (j)–(l) is logarithmic. For comparison, data obtained under the same test conditions for T91 (MGD heat), which has the

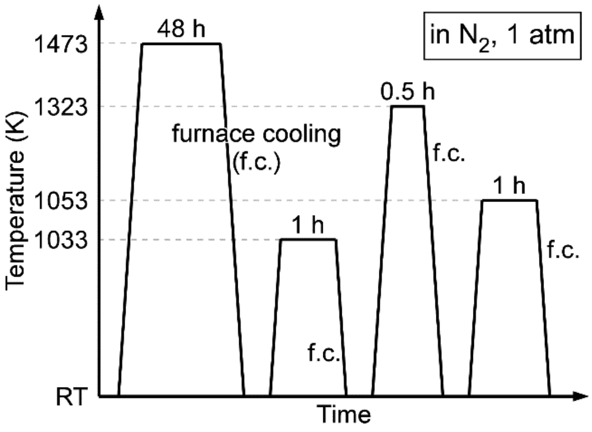

Fig. 1. Thermal history of the solution-nitriding treated sample.

shortest rupture time among the NIMS creep datasheet samples plotted in Fig. 2, are also shown. Compared with the MGD heat sample, the solution-nitriding treated sample exhibited a faster creep rate in the transition region. The MGD heat sample reached the minimum creep rate at a strain of approximately 1%, whereas the solution-nitriding treated sample reached the minimum creep rate at a strain of approximately 3%. In other words, at the start of the acceleration region, the amount of strain was large. Meanwhile, the increase in creep rate with respect to strain in the acceleration region was slightly smaller than that of the MGD heat sample.

Figure 4 shows the relationship between creep rupture time and minimum creep rate for the solution-nitriding treated and NIMS creep datasheet (Monkman–Grant relationship[22]) samples at 923 K. The plot for the solution-nitriding treated sample was not consistent with the approximation line of the NIMS creep datasheet sample,[21] as shown by the gray solid line, and a parallel shift with respect to the side was observed where the product of the rupture time and minimum creep rate increased. The product of the rupture time (t_r) and minimum creep rate ($\dot{\varepsilon}_{\min}$) is expressed as $t_r \cdot \dot{\varepsilon}_{\min} = \left(\sqrt{A} + \sqrt{B}\right)^2$, where the slopes of the tangents ($\mathrm{d}\ln\dot{\varepsilon}/\mathrm{d}\varepsilon$) in the transition and acceleration regions of the creep rate ($\dot{\varepsilon}$)–strain (ε) diagram are $-1/A$ and $1/B$, respectively.[23] The parallel shift of the Monkman–Grant relationship for the solution-nitriding treated sample coincided with the smaller slope of the transition and acceleration regions in the $\dot{\varepsilon}$–ε diagrams (*i.e.*, A and B are large) as shown in Figs. 3(g)–3(i).

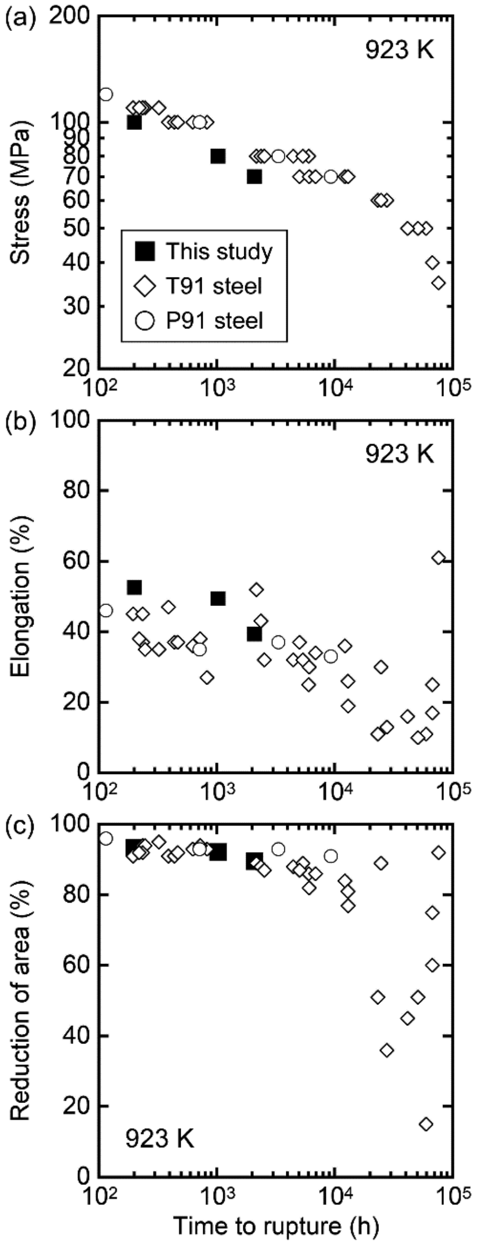

Fig. 2. (a) Stress, (b) elongation and (c) reduction of area vs time to rupture diagram of the solution-nitriding treated sample and conventional modified 9Cr-1Mo steels.[21]

Figures 5(a)–5(c) shows the appearances of the creep-ruptured samples. The width of the gauge portion of the sample projected on the image was measured at 1-mm intervals. The relationship between the reduction of area at each point and the distance from the fracture surface, determined with the assumption that the gauge portion is a perfect circle, is shown in Fig. 5(d). The figures also show plots obtained from the appearance of the MGD heat (rupture time (t_r) = 5 058.5 h, creep rupture elongation (El) = 37%, reduction of area (RA) = 87%), MGF heat (t_r = 6 123.6 h, El = 30%, RA = 82%), and MGG heat (t_r = 6 920.3 h, El = 34%, RA = 86%) samples.[21] The NIMS creep datasheet sample exhibits a large reduction of area only near the fracture surface, and the reduction of area at distances exceeding 10 mm was approximately 15% or less. In contrast, the solution-nitriding treated sample exhibited a large reduction of area throughout the gauge portion, even in the areas away from the fracture surface, with another necking occurring in areas other than the vicinity of the fracture surface, as shown by the arrows in Figs. 5(a)–5(c).

Figure 5(e) shows the creep rupture elongation of the six samples whose reduction of area are shown in Fig. 5(d). The length of the gray and white areas in the bar graph indicates the contribution of deformation to the creep rupture elongation in areas within 10 mm and over 10 mm away from the fracture surface, respectively. The amount of deformation in areas over 10 mm away from the fracture surface was obtained by the following procedure: (1) Width D of the gauge portions measured at 1-mm intervals along the longitudinal direction of the external surface of the creep-ruptured sample. (2) Each 1-mm-wide section from the rupture surface to the flange considered to be a cylinder with diameter D × height of 1 mm. (3) Height h [mm] of a cylinder with the same volume as that of a cylinder with diameter D_0 = 6 mm (diameter of sample before creep test) calculated. (4) Amount of deformation owing to creep of the cylinder defined as 1-h [mm], and the sum of the deformations in each 1-mm-wide section up to the flange calculated as the contribution to the elongation of the 30-mm-long gauge portion of the sample. The contribution of the area within the 10 mm distance from the fracture surface was obtained by calculating the difference between the elongation measured directly from the ruptured sample and the elongation of the area over 10 mm away from the fracture surface. The graph shows that the solution-nitriding treated sample undergoes a large elongation in the area away from the fracture surface shown in gray. The results also confirmed that the majority of the creep rupture elongation was borne by the area near the fracture surface, where significant necking was observed.

3.2. Microstructure of Solution-nitriding Treated Sample

Calculating the diffusion distance x at t = 48 h as x=

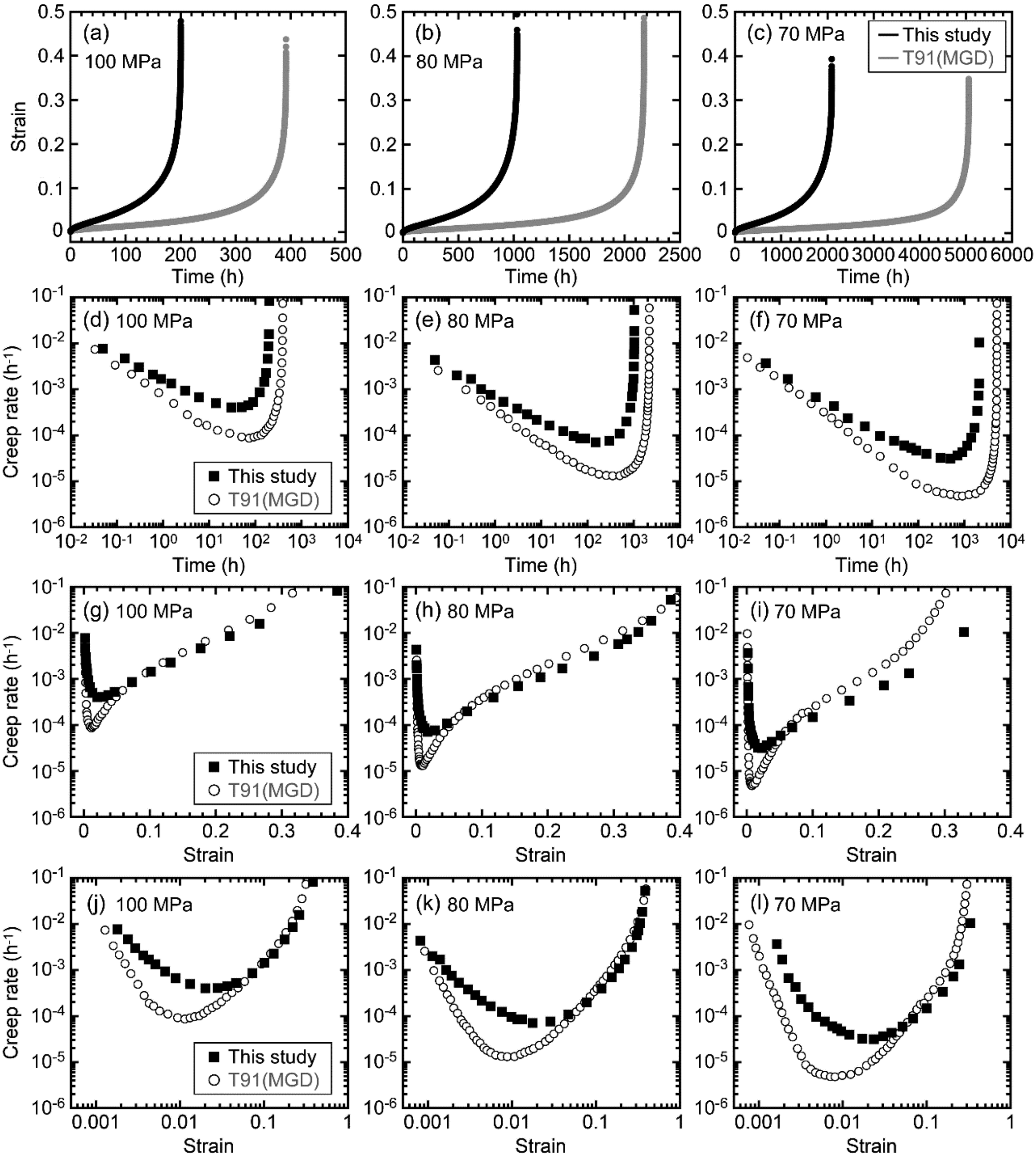

Fig. 3. (a)–(c) Strain vs time curves, (d)–(f) creep rate vs time curves, (g)–(i) creep rate vs strain (linear) curves and (j)–(l) creep rate vs strain (logarithmic) curves of the solution-nitriding treated samples and T91 steel (MGD heat) under (a)(d)(g)(j) 100, (b)(e)(h)(k) 80, and (c)(f)(i)(l) 70 MPa at 923 K.

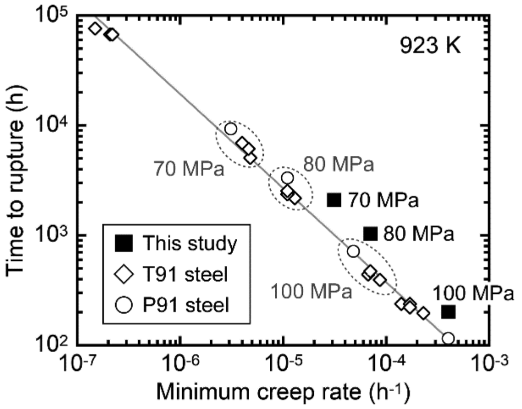

Fig. 4. Relationship between minimum creep rate and time to rupture at 923 K.[21)]

$\sqrt{2Dt}$ using the diffusion coefficient of nitrogen in Fe at 1 473 K ($D = 9.18\times10^{-11}$ [m^2/s][24)]) results in a value of approximately 5.6 mm. Previous research has also confirmed that solution-nitriding heat treatment at 1 473 K for 48 h diffuses nitrogen to a depth of over 3 mm, corresponding to the radius of the gauge portion of a creep test sample with a diameter of 6 mm.[17)] The nitrogen concentration near the surface of the solution-nitriding treated sample in previous research was 0.17 mass%.[17)] The difference in the amount of nitrogen in the precipitates (0.12 mass%) analyzed using the extraction residue was used as a basis to estimate the amount of nitrogen dissolved in the matrix, which was determined to be approximately 0.05 mass%.[17)]

Figure 6(a) shows a SEM image of the solution-nitriding treated sample. The microstructure was found to be tempered martensite with finely dispersed precipitates, and no coarse nitrides larger than a few micrometers were observed. Figure 6(b) shows an inverse pole figure (IPF) map overlaid on the image quality (IQ) map obtained by SEM-EBSD, confirming that the microstructure was martensite. Figure 6(c) shows an IPF map in which the prior austenite grains were reconstructed using the Kurdjumov–Sachs (K–S) orientation relationship based on the orientation information of Fig. 6(b). The black lines in the figure are high-angle grain boundaries with an orientation difference of 15° or more, and the prior austenite grain size of the solution-nitriding treated sample was determined to be approximately 20.9 μm. The prior austenite grain size of the as-received sample, which was approximately 15 μm,[25] was coarsened to several hundred micrometers by solution-nitriding heat treatment at 1 473 K for 48 h.[17] We confirmed that the grain size could be adjusted to the same level as that of the conventional sample through renormalization during the four-stage heat treatment shown in Fig. 1.

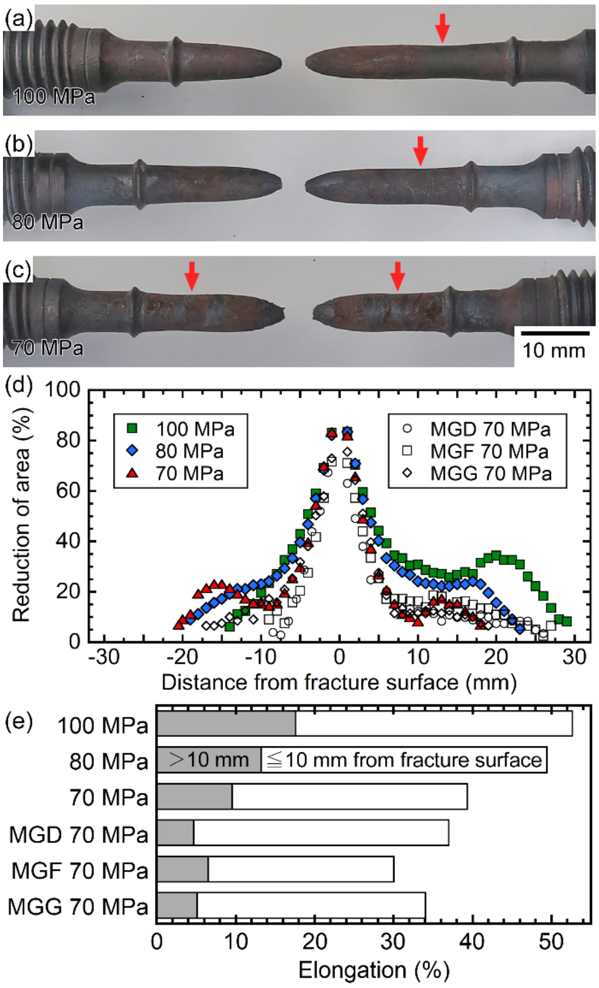

Fig. 5. Appearance of the creep-ruptured specimens ruptured after crept for (a) 200.3 h under 100 MPa, (b) 1 027.9 h under 80 MPa, and (c) 2 092.3 h under 70 MPa at 923 K. (d) Relationship between reduction of area and distance from fracture surface of the creep ruptured specimens. (e) Creep rupture elongation of solution-nitriding treated samples and T91 steels; length of the grey and white color in the bars indicate the contribution of the elongation estimated from the reduction of area at >10 mm and ≦10 mm from fracture surface, respectively. (Online version in color.)

Figure 7(a) shows a STEM bright-field image of the solution-nitriding treated sample. A large amount of precipitates were confirmed in the tempered martensite microstructure. STEM-EDS maps obtained from this field of view are shown in Figs. 7(b)–7(j). The color bar at the top of the elemental map indicates the characteristic X-ray intensity of each element. Figures 7(d), 7(g), and 7(h) shows that the characteristic X-ray intensity of the matrix phase is low in the lower left of the image, which is thought to be owing to the difference in film thickness. Figures 7(b) and 7(c) shows that carbides and nitrides are precipitated at high densities.

X-ray diffraction of the extraction residue of the solution nitriding treated sample confirmed the precipitation of $M_{23}C_6$ (M is mainly Cr) and Cr_2N (containing V, Nb, and Mo).[17] $M_{23}C_6$ also precipitates in normal 9Cr-1Mo-V-Nb steel,[26,27] but Cr_2N precipitates owing to the increase in the amount of nitrogen. Thermo-Calc calculations also show that Cr_2N precipitates when more than 0.05 mass% of nitrogen is added to 9Cr-1Mo-0.2V-0.06Nb-0.001C steel.[28] Because both precipitates mainly contain Cr, distinguishing between the two types of precipitates solely from the Cr map shown in Fig. 7(f) is difficult. However, the Mo distribution shown in Fig. 7(j) was not necessarily consistent with that of Cr, suggesting that multiple maps could be combined to distinguish the precipitates. The Mn map was similar to the Cr map, which was thought to be owing to the similar energy values of the K lines.

We not only confirmed precipitates mainly containing Cr, but also those containing V and Nb, as shown in Figs. 7(e) and 7(i). These precipitates were considered to be MX, which is commonly precipitated in 9Cr-1Mo-V-Nb steel. M is mainly V and Nb, and X is C and N.[26,27] MX was not detected in the X-ray diffraction of extraction residue in previous research,[17] but as described later, MX is the smallest precipitates and also has a low number density. This was thought to be the reason why MX was not picked up by the 200 nm mesh used to collect the residue.

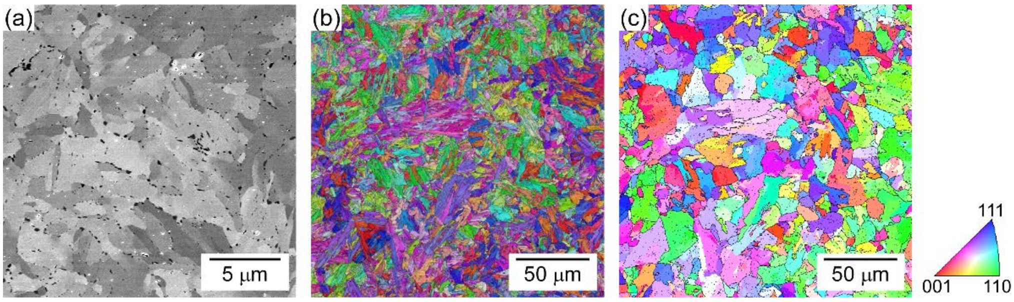

Fig. 6. (a) SEM image, (b) image quality (IQ) overlaid on inverse pole figure (IPF) map, and (c) reconstructed orientation map by K–S orientation relationship overlaid on grain boundary with misorientation of >15 degrees obtained from the solution-nitriding treated sample. (Online version in color.)

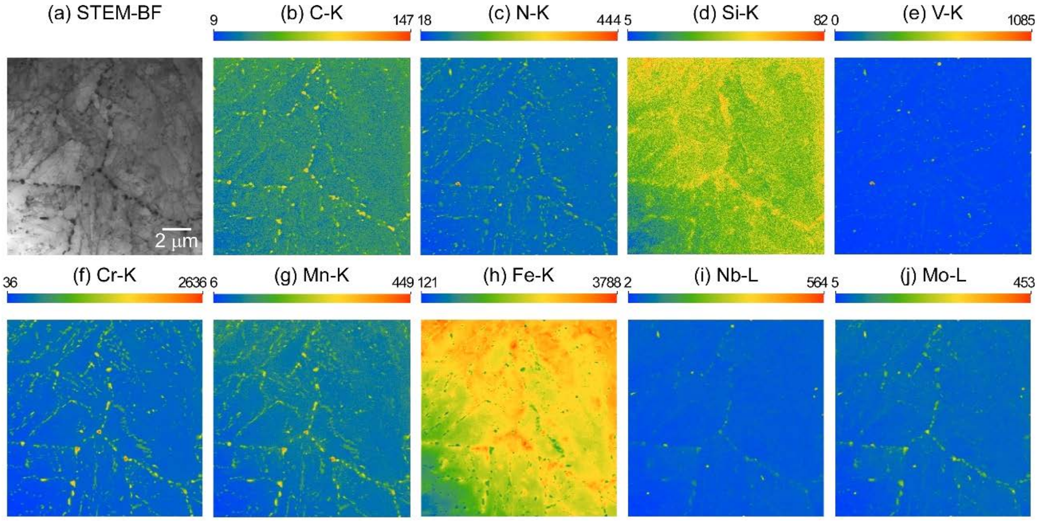

Fig. 7. (a) Bright field STEM image and STEM-EDS mapping for (b) C–K, (c) N–K, (d) Si–K, (e) V–K, (f) Cr–K, (g) Mn–K, (h) Fe–K, (i) Nb–L, and (j) Mo–L of the solution-nitriding treated sample. (Online version in color.)

3.3. Clustering of Precipitates by Multidimensional Scatter Plot Analysis

A scatter diagram analysis plotting the correlation between the characteristic X-ray intensity of each pixel is effective for clustering in cases where multiple phases containing the same element are present, as shown in Fig. 7.[29] Although surface analysis of bulk materials using electron prove micro analyzer (EPMA) has the advantage of obtaining a scatter plot that includes information on the interface, analysis of nano-sized precipitates is difficult because of the scattering of the electron beam in the sample, expanding the area wherein the characteristic X-rays are generated. To the best of our knowledge, no examples of scatter diagram analysis of the thin films using STEM-EDS exist. However, because of the narrow area wherein the characteristic X-rays are generated, the better spatial resolution, and clustering is thought to be possible even for fine precipitates.

Figure 8 shows the scatter plots of the characteristic X-ray intensities of (a) Mo–Cr, (b) V–Cr, and (c) Nb–Cr. Each plot corresponds to the 256 × 256 points of the elemental map shown in Fig. 7. The characteristic X-ray intensities were normalized so that the minimum value was 0 and the maximum value was 1. The region with low characteristic X-ray intensities of Cr, Mo, V, and Nb near the origin corresponded to the matrix. For all scatter plots, the distribution of the plots extends in three directions and are considered to correspond to $M_{23}C_6$, Cr_2N, and MX, respectively.

Consideration of correlations between more alloying elements is thought to increase the accuracy of clustering three types of precipitates that contain a common alloying element using characteristic X-ray intensities as a descriptor. However, visualization of a scatter diagram with four or more dimensions is not possible; thus, data analysis using machine learning is required for clustering.

One clustering algorithm using unsupervised learning is the k-means method.[30] This method allocates k initial values as cluster centers, and all data points are assigned to the cluster center with the highest similarity. The average value of the assigned data points is set as the new cluster center, and all data points are re-assigned to the new cluster center. Repeating this process until the cluster centers converge enables high-dimensional data to be divided into k clusters.

The k-means method generally uses the Euclidean distance (Ed) given by Eq. (1) to represent the similarity between n-dimensional vectors $\boldsymbol{p} = (p_1\ p_2\ p_3\ \dots\ p_n)^{\mathrm{T}}$ and $\boldsymbol{q} = (q_1\ q_2\ q_3\ \dots\ q_n)^{\mathrm{T}}$, where T is the transposed matrix.

$$\mathrm{Ed} = \sqrt{\sum\nolimits_i^n (p_i - q_i)^2}\ . \qquad (1)$$

However, the purpose of this study is to cluster precipitates based on the correlation of characteristic X-ray intensities obtained by STEM-EDS; therefore, a similarity function that considers the element ratio (direction of n-dimensional vector) is more appropriate than the Euclidean distance of characteristic X-ray intensities, which is also affected by the film thickness. The cosine distance (Cd) given by Eq. (2) includes a term that normalizes the inner product of vectors by the product of the absolute values of each vector. In this case, if the angle between two vectors $\boldsymbol{p}$ and $\boldsymbol{q}$ is $\theta = 0°$, then Cd = 0 and similarity is high, whereas if $\theta = 90°$, then Cd = 1 and similarity is low, thus allowing similarity to be evaluated based on the ratio of elements.[31]

$$\mathrm{Cd} = 1 - \frac{\sum\nolimits_i^n q_i p_i}{\sqrt{\sum\nolimits_i^n q_i^2}\sqrt{\sum\nolimits_i^n p_i^2}}\ . \qquad (2)$$

Therefore, the k-means method with the cosine distance as the similarity function was used to classify all data points into four clusters (three types of precipitates and matrix) using the characteristic X-ray intensity of each alloying element stored in each pixel of the 256 × 256 element map shown in Fig. 7 as a descriptor. The details of the clustering in each step are described below. The number of clusters k in each step was selected to maximize the silhouette coefficient.

In Step 1, the nine-dimensional vector consisting of the characteristic X-ray intensities of C, N, Si, V, Cr, Mn, Fe, Nb, and Mo were clustered with $k = 2$. Figures 8(d)–8(f) shows the classification results as two-dimensional scatter plots. The data points clustered near the origin and in other regions were determined to correspond to the matrix and precipitates, respectively.

In Step 2, the data points determined to be precipitates in Step 1 were further clustered with five-dimensional vectors of the characteristic X-ray intensities of N, V, Cr, Nb, and Mo using $k = 2$. C, Si, Mn, and Fe were used in Step 1 because of the difference in intensity between the matrix and precipitates but excluded from the following because the difference between precipitates was small and the effect of film thickness was significant. Figures 8(g)–8(i) shows the clustering results as two-dimensional scatter plots. The vectors were clustered into vectors with less Cr and more

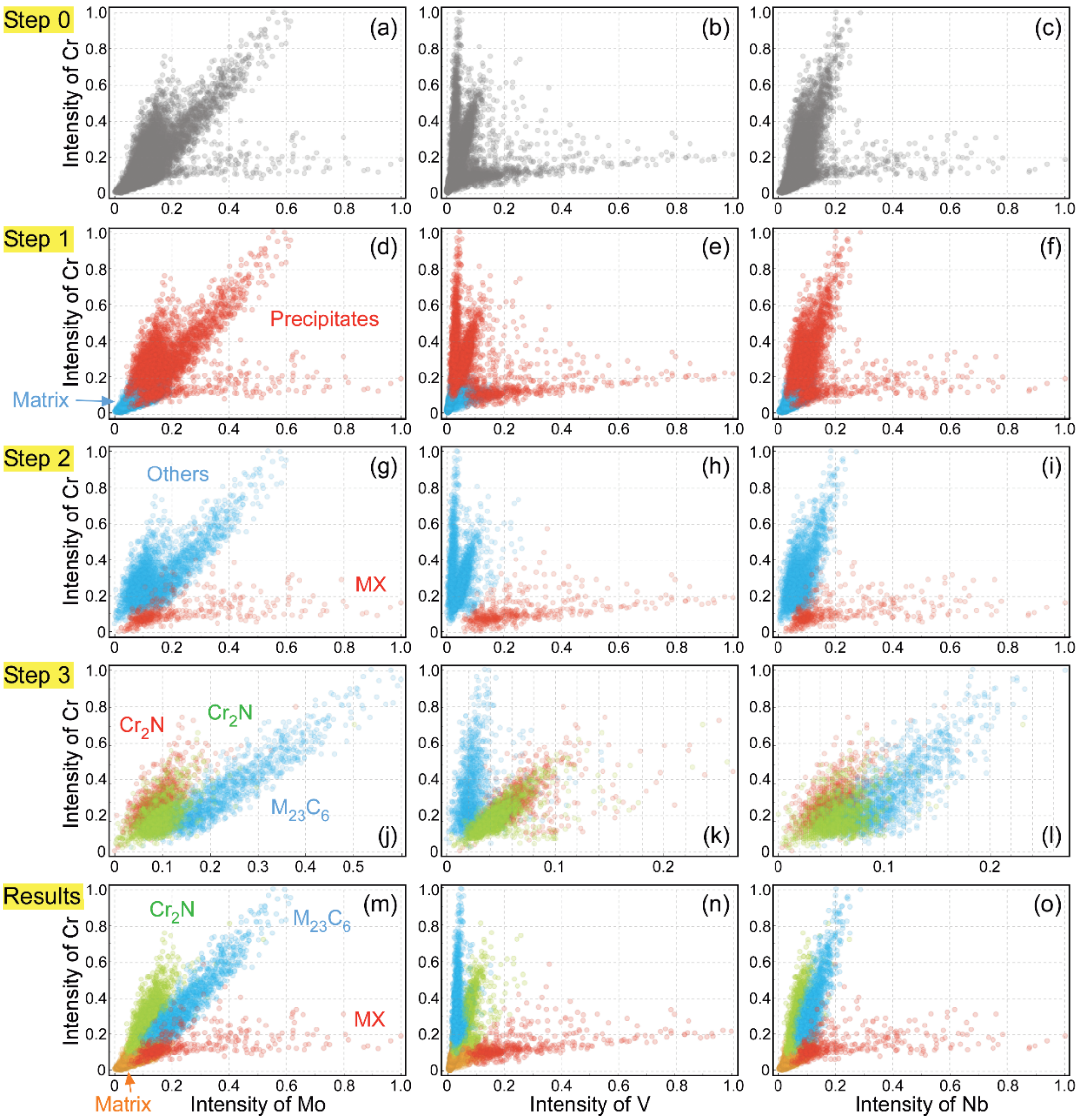

Fig. 8. Scatter diagrams of the X-ray intensity of (a) Mo–Cr, (b) V–Cr, (c) Nb–Cr obtained from STEM-EDS maps of the solution-nitriding treated sample and the progress of the k-means clustering performed in this study: (d)–(f) 1st step, (g)–(i) 2nd step, (j)–(l) 3rd step, and (m)–(o) results of the clustering.

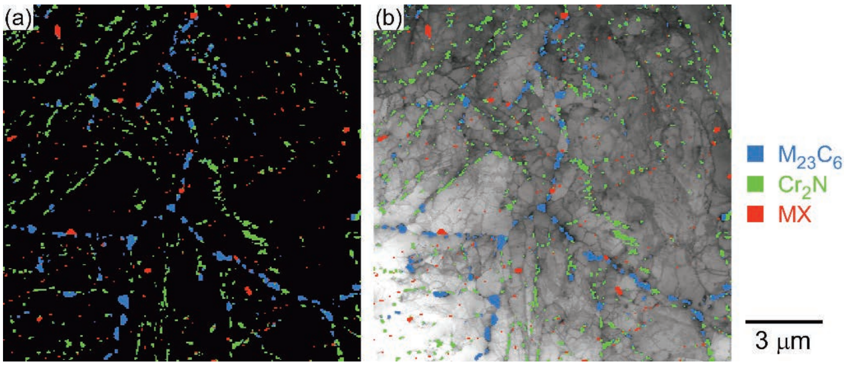

Fig. 9. (a) Clustering results of the precipitation behavior and (b) bright field STEM image overlaid on the clustering results.

Mo, V, and Nb and all other vectors, which were judged to correspond to MX and all other precipitates, respectively.

In Step 3, the data points judged to be other precipitates in Step 2 were clustered into five-dimensional vectors in the same manner as in Step 2. The results indicated that the silhouette coefficient for $k = 3$ was the largest. We judged from the clustering results shown in Figs. 8(j)–8(l) that the vector with more Cr and Mo and less V was $M_{23}C_6$. The other two clusters were both judged to be Cr_2N. Figures 8(m)–8(o) shows the scatter plots reflecting the results of the three-stage clustering. We confirmed that the clustering near the origin and scatter plots extending in three directions were successful.

Figure 9 shows the precipitate map based on the clustering results and the precipitate map overlaid on the STEM bright-field image. The figure shows that a precipitate map could be obtained by machine learning using the X-ray intensity of each alloying element stored in each pixel of the STEM-EDS map as a descriptor. The average size and number density of $M_{23}C_6$, Cr_2N, and MX can be obtained by image processing of this result. However, because one pixel of the element map used in this study corresponded to approximately 54×54 nm^2, precipitates significantly smaller than this size may not have been extracted.

3.4. Microstructural Changes during Creep of Solution-nitriding Treated Sample

Figure 10 shows the (a) SEM image and (b) IQ + IPF map of the gauge portion of the 923 K–70 MPa rupture sample. A comparison with Fig. 6 shows that the precipitates become significantly coarser and that the martensite has recovered and become coarser.

Figure 11 shows the STEM bright-field images and STEM-EDS maps of V, Cr, Nb, and Mo for the gauge portion of the rupture samples at (a)–(e) 100, (f)–(j) 80, and (k)–(o) 70 MPa. The STEM bright-field images show that the lath structure had become coarser owing to creep exposure. **Figure 12** shows the results of clustering the characteristic X-ray intensity data of each pixel as scatter plots of Mo–Cr, V–Cr, and Nb–Cr. As shown in Fig. 8, the scatter plots extend in three directions, and the directions of each vector (ratio of elements) are the same for the creep-ruptured samples under the three conditions, suggesting that there were no changes in the type of precipitates. The clustering of the data for the 80 MPa rupture sample using the k-means method was completed in three stages, as shown in Fig. 8. In contrast, that for the 100 and 70 MPa rupture samples was completed in two stages because $M_{23}C_6$, Cr_2N, and MX were clustered with $k = 3$ in Step 2.

Figure 13 shows a precipitate map drawn based on the clustering results of the X-ray intensity of the STEM-EDS map of the gauge portion of the creep-ruptured sample shown in Fig. 12, superimposed on a STEM bright-field image. Fine precipitates can be seen that were not extracted, but the results showed that the majority of the precipitates that could be recognized in the STEM bright-field image were successfully clustered. It was also found that the precipitates had significantly coarsened.

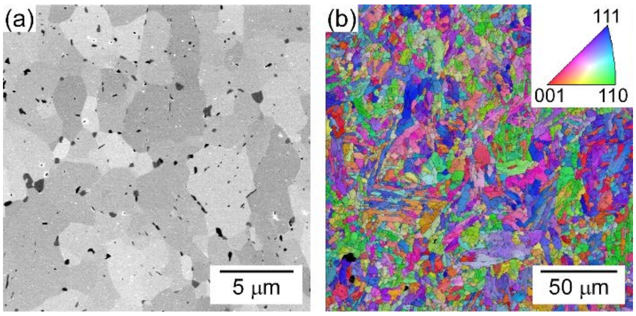

Fig. 10. (a) SEM image and (b) IQ+IPF map of the gauge portion of the creep-ruptured specimen ruptured after crept for 2 092.3 h at 923 K under 70 MPa. (Online version in color.)

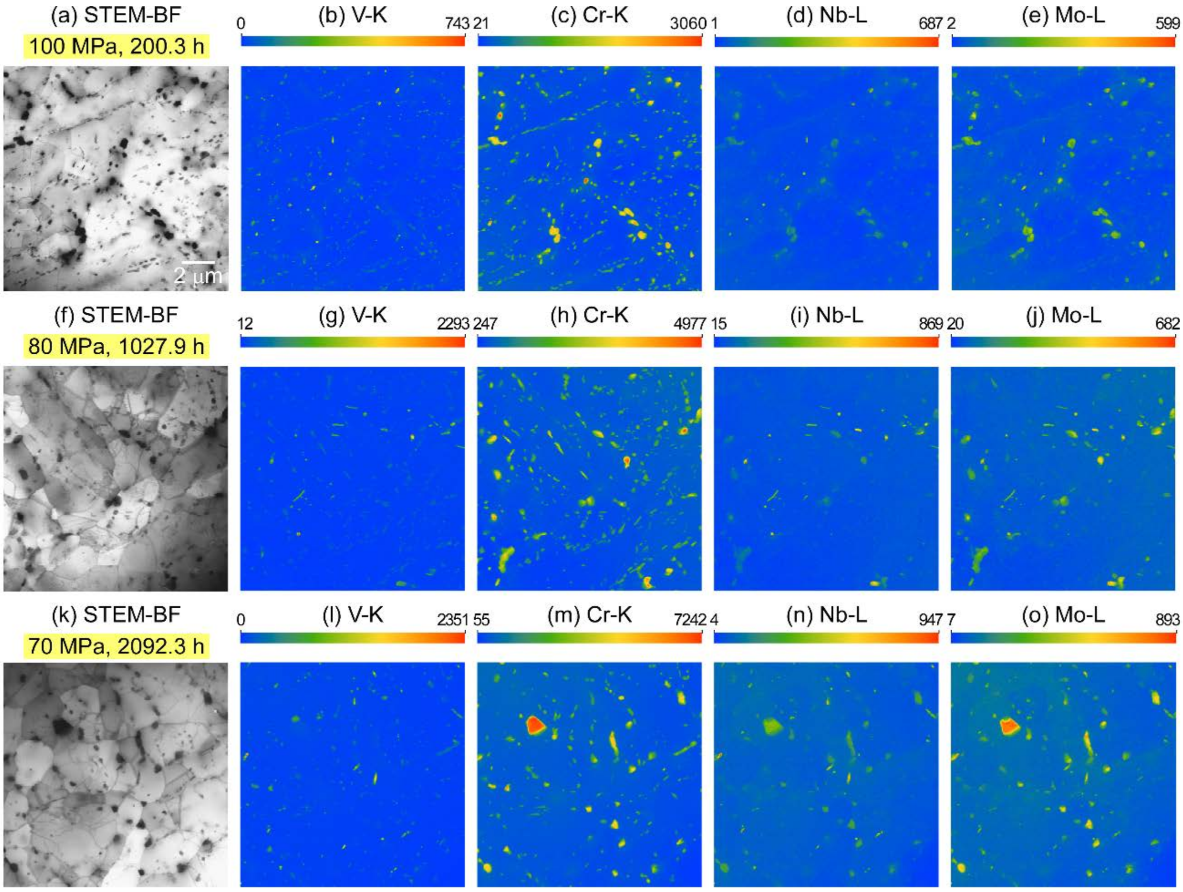

Fig. 11. (a)(f)(k) Bright field STEM image and STEM-EDS mapping for (b)(g)(l) V–K, (c)(h)(m) Cr–K, (d)(i)(n) Nb–K, (e)(j)(o) Mo–K of the creep-ruptured specimen ruptured after (a)–(e) 200.3 h under 100 MPa, (f)–(j) 1 027.9 h under 80 MPa, and (k)–(o) 2 092.3 h under 70 MPa at 923 K. (Online version in color.)

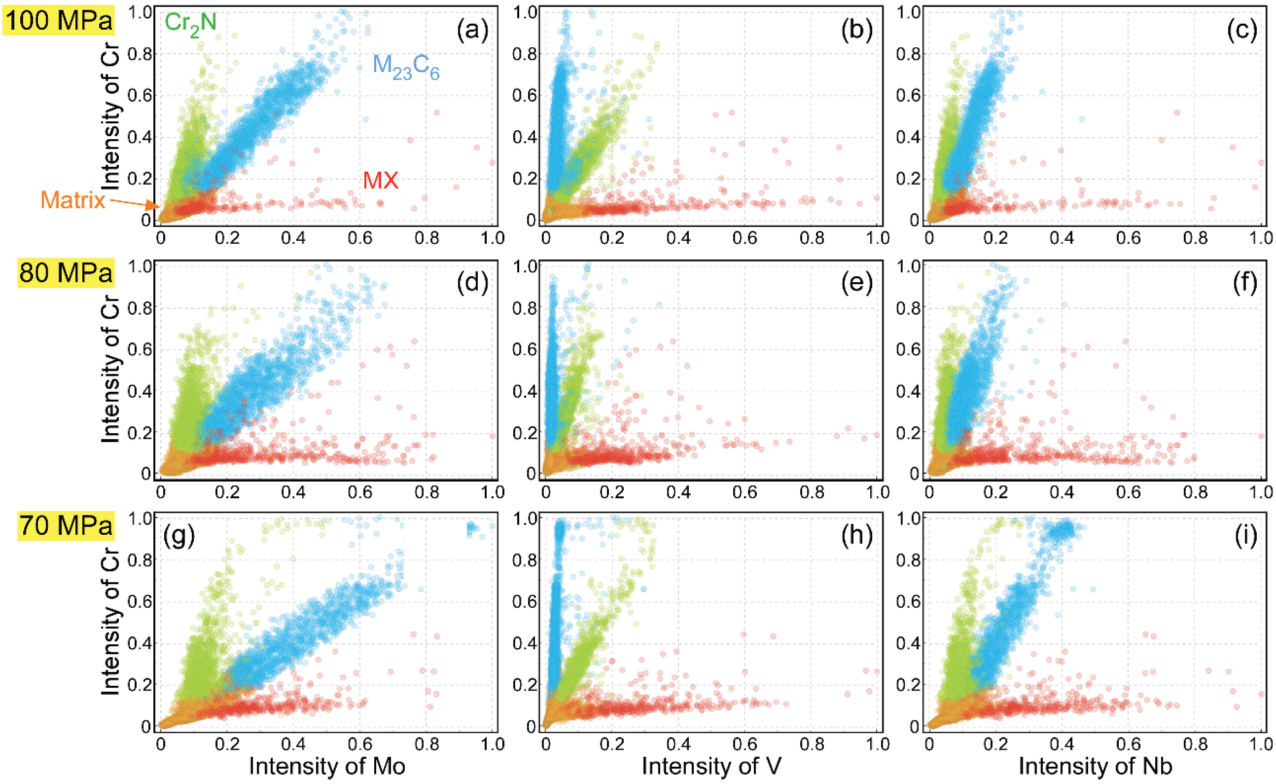

Fig. 12. Scatter diagrams of the X-ray intensity of (a)(d)(g) Mo–Cr, (b)(e)(h) V–Cr, and (c)(f)(i) Nb–Cr clustered by k-means clustering obtained from STEM-EDS maps of the gauge portion of the creep-ruptured specimen ruptured after (a)–(c) 200.3 h under 100 MPa, (d)–(f) 1 027.9 h under 80 MPa, and (g)–(i) 2 092.3 h under 70 MPa at 923 K.

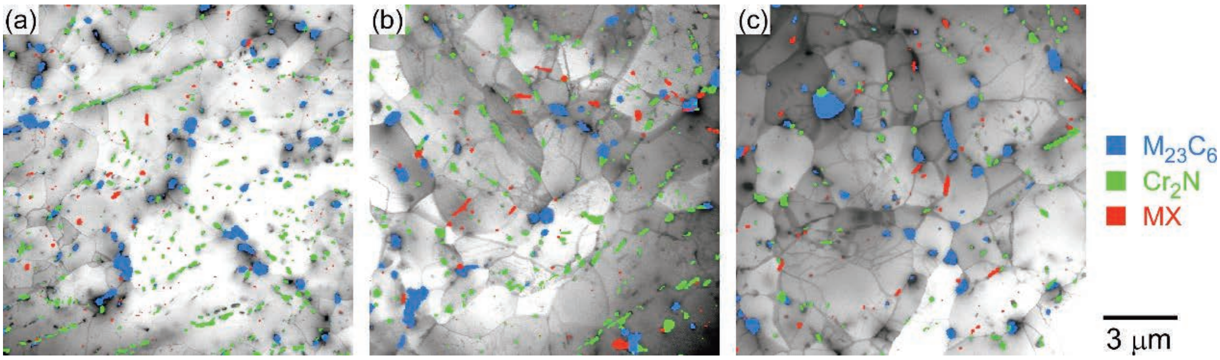

Fig. 13. Bright field STEM images overlaid on the clustering results of the gauge portion of the creep-ruptured specimens ruptured after crept for (a) 200.3 h under 100 MPa, (b) 1 027.9 h under 80 MPa, and (c) 2 092.3 h at 923 K under 70 MPa at 923 K.

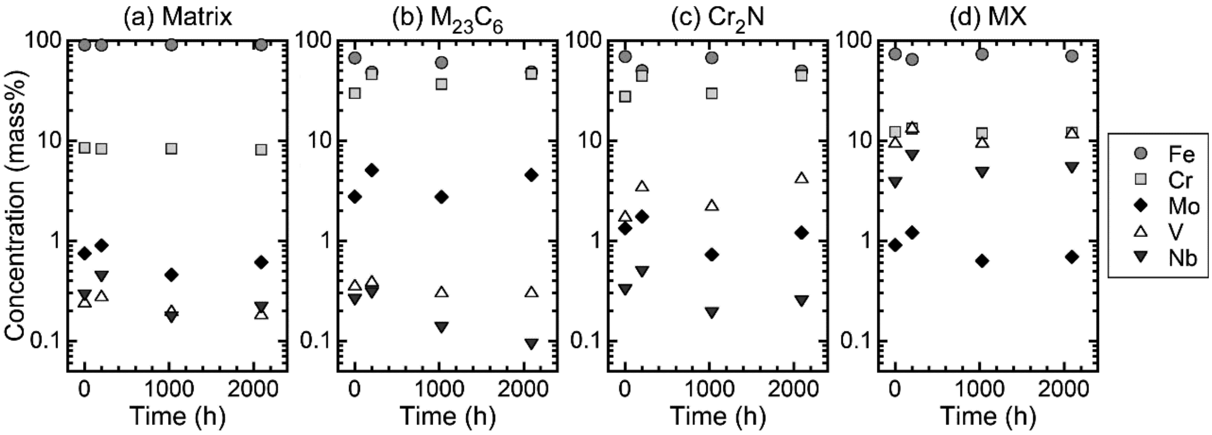

Fig. 14. Changes in average chemical concentration (mass%) of clustered (a) matrix, (b) M$_{23}$C$_6$, (c) Cr$_2$N, and (d) as a function of creep-exposure time.

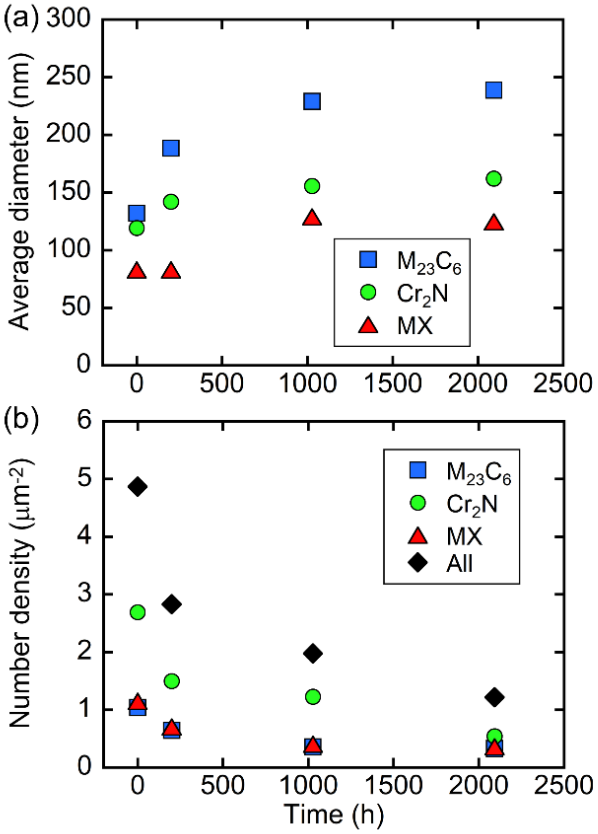

Fig. 15. (a) Average diameter and (b) number density of the precipitates identified by the k-means clustering as a function of creep-exposure time. (Online version in color.)

Figure 14 shows the average compositions of (a) the matrix, (b) $M_{23}C_6$, (c) Cr_2N, and (d) MX obtained from the clustering results. The quantitative analysis results of each pixel in the STEM-EDS map were normalized so that the sum of the Fe, Cr, Mo, V, and Nb concentrations was 100%. Our study involved the analysis of thin films prepared by electrolytic polishing; therefore, the average composition of each precipitate and the clustered pixels is thought to be influenced by the adjacent matrix phase. Therefore, the change in the average composition of each precipitate over time cannot be quantitatively discussed here. Meanwhile, because the average composition was within a certain range, the clustering is thought to have been conducted with relatively high accuracy. Accurately evaluating the change in average composition over time without the influence of the matrix phase requires analyzing samples prepared by the extraction replica method.

Figure 15(a) shows the relationship between the average particle size of the clustered precipitates and rupture time. The particle size was defined as the diameter of a circle equivalent to the sum of the areas of consecutive pixels clustered as the same precipitate, and the average values were plotted. The as-tempered sample (0 h) of $M_{23}C_6$ had the largest average particle size at approximately 130 nm, and MX had the smallest at approximately 80 nm. The precipitates coarsened with increased creep rupture time, and when the rupture time was approximately 2 092.3 h, the average particle sizes of $M_{23}C_6$, Cr_2N, and MX were approximately 240, 160, and 125 nm, respectively.

Figure 15(b) shows the relationship between the number density of clustered precipitates and time to rupture. The possibility that fine precipitates were not clustered needs to be considered. However, the number density of Cr_2N was the highest in the as-tempered sample, and the number densities of $M_{23}C_6$ and MX were similar. The sum of the number densities of the three types of precipitates was approximately 5 μm^{-2} in the as-tempered sample. The number density of the precipitates decreased monotonically with increasing creep rupture time. The rate of decrease was largest for Cr_2N, and the number density ruptured after 2 092.3 h was decreased to the same level as that of $M_{23}C_6$ and MX.

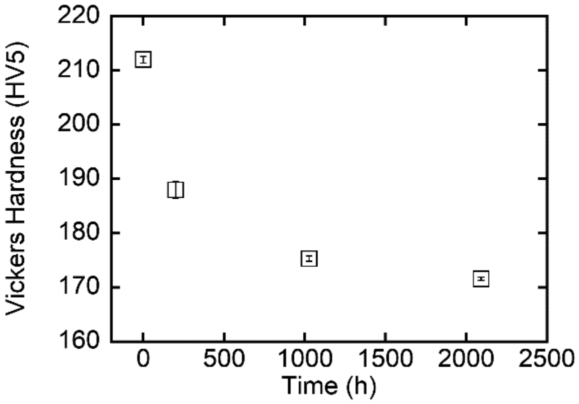

Fig. 16. Vickers hardness of the gauge portion of the samples as a function of creep-exposure time.

Figure 16 shows the relationship between the Vickers hardness of the gauge portion of the creep-ruptured sample and rupture time. The standard deviation of the three points used to measure the average value is shown as an error bar. The initial hardness was HV = 212, which was smaller than the hardness of normal 9Cr-1Mo-V-Nb steel (HV of approximately 230[18)]). The hardness decreased as a result of creep, and the hardness decreased further with longer rupture time. The hardness of the 923 K creep-ruptured sample composed of 9Cr-1Mo-V-Nb steel with an initial hardness of HV = 235 was reported to be HV = 185, 180, and 175 at rupture times of approximately 200, 1 000, and 5 000 h, respectively,[32)] which is consistent with the values of the solution-nitriding treated sample obtained in this study.

4. Discussion

We clarified the change in precipitation behavior associated with solution nitriding and creep by analyzing and clustering the multidimensional scatter plot of characteristic X-ray intensity obtained by STEM-EDS mapping of a solution-nitriding treated sample using a machine learning technique. For reference, Fig. S1 (Supporting Information) shows the STEM bright-field image and STEM-EDS map (note: the acquisition magnification differs from Figs. 7 and 11) of the as-received MGD heat sample, and Fig. S2 (Supporting Information) shows the scatter plot of the characteristic X-ray intensity and clustering results. In the case of normal 9Cr-1Mo-V-Nb steel without solution nitriding, the scatter plot distributions extend in two directions, which corresponds to $M_{23}C_6$ and MX, respectively. This differs from the scatter plot of the solution-nitriding treated sample, where Cr_2N precipitated and the plot distributions extend in three directions (Figs. 8 and 12), indicating that the precipitation behavior changed owing to solution nitriding. Figure S3 (Supporting Information) shows the precipitate map obtained from the clustering results. The average particle sizes of MX and $M_{23}C_6$ obtained from these results were

53 and 120 nm, respectively, and a comparison with the solution-nitriding treated sample shown in Fig. 15 revealed that MX was finer and $M_{23}C_6$ was similar.

A previous study reported that the number density of MX in as-tempered 9Cr-1Mo-V-Nb steel was approximately 10 μm^{-2} and that had been maintained up to a rupture time of approximately 5 000 h at 923 K.[33] The number density of $Ms_{23}C_6$ in as-tempered 9Cr-1Mo-V-Nb steel was also approximately 1.5–2 μm^{-2}, but previous research indicated that this decreases to 0.5 μm^{-2} in creep-ruptured samples had a rupture life of several thousand hours at 923 K.[18] The number densities of MX and $M_{23}C_6$ in the as-received MGD heat, as determined by clustering the scatter plots of the STEM-EDS maps of three fields as shown in Fig. S3 (Supporting Information), were 5.4 and 4.2 μm^{-2}, respectively, which was accurate within approximately half to double the literature value.[33] The underestimation of the number density of MX was thought to be owing to the inability to extract fine precipitates by clustering the scatter plot. Meanwhile, the overestimation of the number density of $M_{23}C_6$ was thought to be owing to the analysis of a map obtained from a relatively narrow field of view (4.5 × 4.5 μm^2) centered on the prior austenite grain boundary where the amount of $M_{23}C_6$ precipitates is large. The number density of precipitates in the solution-nitriding treated sample may have been underestimated because fine precipitates could not be clustered, but even in such cases, the number density of MX and $M_{23}C_6$ in the as-tempered condition was approximately 1 μm^{-2} and that of all precipitates including Cr_2N was approximately 5 μm^{-2}, which was clearly lower than that of the normal sample. This results in the lower initial hardness (Fig. 16). This change in precipitation behavior was thought to be owing to the precipitation of Cr_2N resulting from the increase in nitrogen addition and consumption of Cr and N, which in turn lowered the number density of $M_{23}C_6$ and MX.

The coarsening behavior of $M_{23}C_6$ precipitated in the solution-nitriding treated sample was in good agreement with that reported for 9Cr-1Mo-V-Nb steel,[33] but the coarsening of MX was faster than that reported in[33] (Fig. 15(a)). This suggested that the increase in nitrogen content promoted MX coarsening.[34] The number density of all precipitates also decreased to approximately 1 μm^{-2} after crept for 2 092.3 h. This was an order of magnitude smaller than the sum of the number densities of $M_{23}C_6$[18] and MX[33] in the conventional 9Cr-1Mo-V-Nb steel with the same rupture time. Therefore, the increase in the creep rate and minimum creep rate in the transition period of the solution-nitriding treated sample and subsequent decrease in rupture time were thought to have been owing to the change in precipitation behavior accompanying solution nitriding, which in turn resulted in a smaller contribution of precipitation strengthening compared to the conventional steels. Yamasaki *et al.*[6] speculated that the contribution of Cr_2N to creep strength was smaller than that of MX, presumably owing to the lower structural stability of Cr_2N during creep and its rapid coarsening. Therefore, the creep strength was thought to decrease more significantly on the long-term side. The above results suggest that the creep strength of 9Cr-1Mo-V-Nb steel may be affected in cases where long-term use under ammonia atmosphere results in a large amount of nitrogen being dissolved into the sample.

The addition of nitrogen to 9Cr-1Mo-V-Nb steel using the solution-nitriding method resulted in a decrease in creep strength but an increase in creep rupture elongation compared to the NIMS creep datasheet samples (Fig. 2). At the start of accelerated creep, the strain was large, and the rate of increase of the creep rate with respect to the strain in the acceleration region was smaller than that of the NIMS creep datasheet sample (Fig. 3).

Kushima *et al.*[32] reported that creep-ruptured samples of 9Cr-1Mo-V-Nb steel experienced preferential recovery near the prior austenite grain boundaries in the low-stress, long-term region. The occurrence of such non-uniform structural changes decreases the contribution of intragranular deformation to creep strain; thus, accelerated creep begins at a small strain value and creep rupture elongation decreases.[32] These results suggest that, in the same manner as the elongation of solution-nitriding treated samples in room temperature tensile tests improved in previous research,[17] the uniform deformability also increased in creep, and the strain amount at the start of accelerated creep and creep rupture elongation increased slightly owing to the strain being borne by the entire microstructure.

Hatakeyama *et al.*[35] conducted creep tests after changing the initial structure of austenitic heat-resistant steel (25Cr-20Ni-Nb-N steel), in which significant intergranular fracture occurs, by pre-aging. They reported that increasing the grain boundary coverage rate by $M_{23}C_6$ to approximately 90% resulted in a significant decrease in the rate of increase of creep rate with respect to strain in the acceleration region and an improvement in creep rupture elongation. An increase in a matrix/$M_{23}C_6$ interface with an orientation relationship owing to an increase in the grain boundary coverage rate suppressed the percolation of random grain boundaries without precipitates and the matrix/$M_{23}C_6$ interface without an orientation relationship. In this case, even if a crack occurred at the grain boundary, creep would continue without fracture, allowing creep deformation to occur throughout the gauge portion and a large elongation to be achieved in the acceleration region.[35] Grain boundary fracture is generally not prominent in 9Cr-1Mo-V-Nb steel, and the necked region is responsible for most of the creep rupture elongation as shown in Fig. 5(e), making the effect unclear. However, a comparison with the NIMS creep datasheet sample shows that the amount of deformation in the gauge portion of the solution-nitriding treated sample was larger than that of the NIMS creep datasheet sample (Figs. 5(d) and 5(e)), suggesting that the deformation was borne by the entire gauge portion and uniform deformability increased. In other words, the results suggested that both the (1) increase in microscopic uniform deformability at the martensite hierarchical structure level and (2) increase in macroscopic uniform deformability at the creep specimen level increased the creep rupture elongation of the solution-nitriding treated sample. Further study is needed for clarifying the mechanism of the increase in uniform deformability owing to solution nitriding.

5. Conclusion

We investigated the changes in creep deformation behavior and precipitation behavior of nitrogen-added 9Cr-1Mo-V-Nb steel by solution nitriding. Solution nitriding resulted in 0.17 mass% of nitrogen dissolution, and tempering resulted in the precipitation of not only $M_{23}C_6$ and MX but also Cr_2N. We proposed a method for clustering the matrix phase and precipitates by extending the scatter diagram analysis to multiple dimensions and machine learning the characteristic X-ray intensity of each alloying element at each pixel of the STEM-EDS map as a descriptor. A comparison with normal 9Cr-1Mo-V-Nb steel showed that the precipitate number density of the solution-nitriding treated sample was smaller and the rate of decrease in the number density of Cr_2N was greater than that of other precipitates;

therefore, the creep strength of the solution-nitriding treated sample was lower than that of the normal sample. The creep curve shape also changed, suggesting an increase in uniform deformability. The excessive addition of nitrogen reduces creep strength because of the precipitation of Cr_2N, which has low structural stability. This may influence creep strength when 9Cr-1Mo-V-Nb steel is used for an extended period under ammonia atmosphere. Nevertheless, nitrogen is an effective additive element in terms of solid solution strengthening, ductility, and oxidation resistance; thus, properties may be improved by adding an appropriate amount of nitrogen and by controlling precipitation of nitrides.

Supporting Information

Bright field STEM image and STEM-EDS mapping for V–K, Cr–K, Nb–K, and Mo–L, Scatter diagram of the X-ray intensity of Mo–Cr, V–Cr, Nb–Cr obtained from the STEM-EDS maps, and clustered precipitates map of the as-received T91 (MGD heat).

This material is available on the Journal website at https://doi.org/10.2355/isijinternational.ISIJINT-2025-211.

Declaration of Conflict of Interest

We declare that there are no conflicts of interest regarding the performance of this research.

Acknowledgments

The creep tests were conducted by Mr. Yasushi Taniuchi, Dr. Kaoru Sekido, and Mr. Takehiro Nojima of the Creep Data Unit, Research Network and Facility Services Division, National Institute for Materials Science. The microstructural observations were conducted with the support of Mr. Taku Moronaga, Ms. Yuka Hara, and Ms. Akiko Nakamura of the Electron Microscopy Unit, Research Network and Facility Services Division, National Institute for Materials Science. This research was conducted as part of activities conducted by the Japan Institute of Metals and Materials Young Researchers' Group "Research Group on Environmentally Resistant Structural Metal Materials for a Zero-CO_2 Emission Society".

REFERENCES

1) F. Masuyama: *ISIJ Int.*, **41** (2001), 612. https://doi.org/10.2355/isijinternational.41.612
2) A. Ohji: *Therm. Nucl. Power Gener. Conv.*, **72** (2021), 498 (in Japanese). https://doi.org/10.14942/tenpes.72.498
3) T. Takase: *Tetsu-to-Hagané*, **66** (1980), 1423 (in Japanese). https://doi.org/10.2355/tetsutohagane1955.66.9_1423
4) ASME Boiler and Pressure Vessel Code, Section II. Part D, American Society of Mechanical Engineers (ASME), New York, NY, (2019).
5) Y. Tsuchida, Y. Naruoka and Y. Tokunaga: *J. At. Energy Soc. Jpn.*, **38** (1996), 393. https://doi.org/10.3327/jaesj.38.393
6) S. Yamasaki, M. Mitsuhara and H. Nakashima: *ISIJ Int.*, **58** (2018), 1146. https://doi.org/10.2355/isijinternational.ISIJINT-2017-758
7) S. Yamasaki, M. Mitsuhara, H. Nakashima and K. Kimura: *Tetsu-to-Hagané*, **109** (2023), 167 (in Japanese). https://doi.org/10.2355/tetsutohagane.TETSU-2022-065
8) S. Matsubara, T. Yamaguchi and F. Masuyama: *ISIJ Int.*, **58** (2018), 2095. https://doi.org/10.2355/isijinternational.ISIJINT-2018-246
9) N. Nakamura and S. Takaki: *ISIJ Int.*, **36** (1996), 922. https://doi.org/10.2355/isijinternational.36.922
10) T. Onomoto, Y. Terazawa, T. Tsuchiyama and S. Takaki: *ISIJ Int.*, **49** (2009), 1246. https://doi.org/10.2355/isijinternational.49.1246
11) T. Tsuchiyama, Y. Fujii, Y. Terazawa, K. Nakashima, T. Ando and S. Takaki: *ISIJ Int.*, **48** (2008), 861. https://doi.org/10.2355/isijinternational.48.861
12) M. Demura: *Tetsu-to-Hagané*, **109** (2023), 490 (in Japanese). https://doi.org/10.2355/tetsutohagane.TETSU-2022-122
13) T. Hatakeyama, K. Sawada, T. Hara, K. Sekido and K. Kimura: *Scr. Mater.*, **200** (2021), 113904. https://doi.org/10.1016/j.scriptamat.2021.113904
14) D. S. Bulgarevich, S. Tsukamoto, T. Kasuya, M. Demura and M. Watanabe: *Sci. Rep.*, **8** (2018), 2078. https://doi.org/10.1038/s41598-018-20438-6
15) D. S. Bulgarevich, S. Tsukamoto, T. Kasuya, M. Demura and M. Watanabe: *Sci. Technol. Adv. Mater.*, **20** (2019), 532. https://doi.org/10.1080/14686996.2019.1610668
16) H. Kim, J. Inoue and T. Kasuya: *Sci. Rep.*, **10** (2020), 17835. https://doi.org/10.1038/s41598-020-74935-8
17) S. Ida and K. Yoshimi: *Tetsu-to-Hagané*, **110** (2024), 1122 (in Japanese). https://doi.org/10.2355/tetsutohagane.TETSU-2024-064
18) K. Sawada, K. Sekido, K. Kimura, K. Arisue, M. Honda, N. Komai, N. Fukuzawa, T. Ueno, N. Shimohata, H. Nakatomi, K. Takagi, T. Kimura, K. Nomura and K. Kubushiro: *ISIJ Int.*, **60** (2020), 382. https://doi.org/10.2355/isijinternational.ISIJINT-2019-358
19) J. Demšar, T. Curk, A. Erjavec, Č. Gorup, T. Hočevar, M. Milutinovič, M. Možina, M. Polajnar, M. Toplak, A. Starič, M. Štajdohar, L. Umek, L. Žagar, J. Žbontar, M. Žitnik and B. Zupan: *J. Mach. Learn. Res.*, **14** (2013), 2349.
20) J. Schindelin, I. Arganda-Carreras, E. Frise, V. Kaynig, M. Longair, T. Pietzsch, S. Preibisch, C. Rueden, S. Saalfeld, B. Schmid, J.-Y. Tinevez, D. J. White, V. Hartenstein, K. Eliceiri, P. Tomancak *et al.*: *Nat. Methods*, **9** (2012), 676. https://doi.org/10.1038/nmeth.2019
21) NIMS Creep Data Sheet, No. 43A, National Institute for Materials Science (NIMS), Tsukuba, (2014).
22) F. C. Monkman and N. J. Grant: *ASTM Proc.*, **56** (1956), 593.
23) K. Maruyama: *Tetsu-to-Hagané*, **105** (2019), 767 (in Japanese). https://doi.org/10.2355/tetsutohagane.TETSU-2019-006
24) P. Grieveson and E. T. Turkdogan: *Trans Metall. Soc. AIME*, **230** (1964), 407.
25) K. Watanabe, S. Ida and K. Yoshimi: *Tetsu-to-Hagané*, **107** (2021), 825 (in Japanese). https://doi.org/10.2355/TETSUTOHAGANE.TETSU-2021-033
26) K. Maruyama, K. Sawada and J.-i. Koike: *ISIJ Int.*, **41** (2001), 641. https://doi.org/10.2355/isijinternational.41.641
27) K. Sawada, H. Kushima, M. Tabuchi and K. Kimura: *Mater. Sci. Eng.: A*, **528** (2011), 5511. https://doi.org/10.1016/j.msea.2011.03.073
28) S. Yamasaki: Ph.D. Thesis, Kyushu University, (2013), (in Japanese). https://doi.org/10.15017/1441288
29) T. Kimura, T. Sugizaki, K. Nishida, N. Ishikawa and S. Tanuma: *J. Jpn. Inst. Met.*, **68** (2004), 8 (in Japanese). https://doi.org/10.2320/jinstmet.68.8
30) K. P. Sinaga and M.-S. Yang: *IEEE Access*, **8** (2020), 80716. https://doi.org/10.1109/ACCESS.2020.2988796
31) Y. Iwasaki: Materials Informatics: Zairyou Kaihatsu no Tame no Kikai Gakusyuu Chou Nyuumon (A Beginner's Guide to Machine Learning for Materials Development), The Nikkan Kogyo Shimbun, Tokyo, (2019), 43 (in Japanese). ISBN9784526079863
32) H. Kushima, K. Kimura and F. Abe: *Tetsu-to-Hagané*, **85** (1999), 841 (in Japanese). https://doi.org/10.2355/tetsutohagane1955.85.11_841
33) K. Suzuki, S. Kumai, H. Kushima, K. Kimura and F. Abe: *Tetsu-to-Hagané*, **89** (2003), 691 (in Japanese). https://doi.org/10.2355/tetsutohagane1955.89.6_691
34) K. Sawada, M. Taneike, K. Kimura and F. Abe: *ISIJ Int.*, **44** (2004), 1243. https://doi.org/10.2355/isijinternational.44.1243
35) T. Hatakeyama, K. Sawada, K. Sekido and K. Kimura: *Mater. Sci. Eng.: A*, **882** (2023), 145487. https://doi.org/10.1016/j.msea.2023.145487